

Design Study of a Line Integrated Thomson Scattering System for TST-2 Spherical Tokamak Device^{*)}

Akira EJIRI, Yu-Ting LIN, Seowon JANG, Yi PENG, Kouji SHINOHARA, Takeshi IDO¹⁾,
Kaori KONO¹⁾ and Yoshihiko NAGASHIMA¹⁾

The University of Tokyo, Kashiwa 277-8561, Japan

¹⁾*Kyushu University, Kasuga 816-8580, Japan*

(Received 16 December 2022 / Accepted 6 March 2023)

A design study of a line integrated Thomson scattering (TS) system with a complete backscattering configuration has been performed to clarify practical problems. Installation on the TST-2 spherical tokamak was assumed, and an optical system design with ready-made components, are adopted. Some practical aspects, such as aberration, masking effect of the laser combining mirror, misalignment are investigated by ray tracing calculations. The performance of density profile reconstruction was also investigated. It was found that a tangential-multi-chord measurement configuration on the midplane shows a good effective localization, and error enhancement in the reconstruction is small. In addition, the efficiency of the system is about an order of magnitude larger than the present conventional TS system in TST-2. The attractiveness of the line integrated TS measurements was demonstrated.

© 2023 The Japan Society of Plasma Science and Nuclear Fusion Research

Keywords: Thomson scattering measurement, line integrated measurement, backscattering, profile reconstruction

DOI: 10.1585/pfr.18.2402025

1. Introduction

In nuclear fusion reactors, plasma diagnostics are expected to be limited due to the harsh environment and due to the small available space. The large neutron fluence, strong erosion and impurity deposition would cause serious damage to optical components, such as window, fiber, and these should be located far from the plasma. In addition, most of the first wall area is devoted to tritium blanket modules, and the area available for plasma diagnostics is expected to be less than about 1% of the whole area. The first mirror is one of key components for optical measurements in ITER and also in demo reactors. According to the analysis for EU DEMO [1], the first mirror should be located behind a thin tube, of which length L and radius r should satisfy the ratio $L/r > 50$ for visible light measurements. Using such a thin tube, the neutral particle flux from plasma is reduced by the neutral particles in the tube, and the degradation of a (metallic) mirror becomes tolerable. In such a case, the solid angle seen from plasma becomes smaller than $\pi r^2/L^2 < 1.3 \times 10^{-3}$ sr. This could be a serious problem for a conventional Thomson scattering (TS) measurement, in which laser scattering light is collected by the first mirror.

Since the collected photon number is proportional to the product of solid angle and scattering length, which is the length of the injected laser beam contributing to a

signal, one may increase the scattering length to compensate the reduced solid angle. A line integrated complete backscattering TS configuration utilizes a long scattering length, and a feasibility study for JA DEMO [2] has shown promising performance [3]. Here, we use the word complete backscattering to denote 180° scattering for the principal ray of the collection optics. The target of the measurements is the edge pedestal pressure profile, and a laser is injected from an upper port. The laser beam is aligned to the optical axis of the collection optics, which is a spherical mirror in this case. The beam is tangent to a magnetic flux surface, which provides a long effective scattering length. Since the measurement is roughly a line integrated measurement, a multi-chord measurement and a profile reconstruction are necessary. The advantages and disadvantages for the complete backscattering configuration are as follows. The effective scattering length for a given spatial resolution along the minor radius becomes long when the beam (and optical axis) is tangent to a magnetic surface, and this enables better signal to noise (SN) ratio than the conventional scattering angle configuration. In general, profile reconstructions from a multi-chord line integrated measurement induces an enhancement of error. Fortunately, in the case of the edge pedestal measurement, the steep density gradient along the minor radius mitigates the error enhancement in reconstruction.

Although the feasibility study has shown good SN ratios [3], a practical configuration was not considered. A realistic optical arrangement including specifications of the

author's e-mail: ejiri@k.u-tokyo.ac.jp

^{*)} This article is based on the presentation at the 31st International Toki Conference on Plasma and Fusion Research (ITC31).

components should be considered to estimate the efficiency of the collection optics and to clarify practical problems and the factors limiting the performance. One approach is designing a system which is applicable to an existing fusion device. Then one can estimate the quantitative performance under a practical situation, such as finite alignment accuracy. In addition, one can compare the performances between a conventional TS configuration and the new TS configuration under the same conditions.

In this paper, we report a design study of a line integrated TS system for the TST-2 spherical tokamak device. The features of the complete backscattering optics is described in Sec. 2. A lens optics design and its performance are shown. The performance of density profile reconstruction is shown in Sec. 3. Conclusions are given in Sec. 4.

2. Features of Complete Backscattering Optics

In this section, the features of the optics are shown. Firstly, analytic expression of the solid angle along the laser beam (which is aligned to the optical axis of the collection optics) and numerical results for a simple spherical mirror optics is shown. In the former we assume an ideal optical system for given first optical component's diameter and location and for given fiber's diameter and numerical aperture. Secondly, two collection optics designs which can be installed into the TST-2 spherical tokamak [4] are described, and their solid angle profiles are discussed considering some practical effects.

Figure 1 shows a schematic drawing of a complete backscattering configuration with a lens (diameter D_L , focal length f) and a fiber (diameter d , numerical aperture NA). Here, we assume the lens is an ideal one, that is a thin lens without aberration. Firstly, we assume that the laser beam size is zero, and we consider the collection efficiency of the scattering light as a function of coordinate x along the laser. The scattering light passing through the lens located at $x = f_1$ and the fiber entrance aperture located at $x = f_1 + f_2$ contributes to the signal as long as the incident angle to the fiber aperture is within the numerical aperture. Here, we set the origin $x = 0$ so that the light emitted from the origin is focused at the fiber. In the

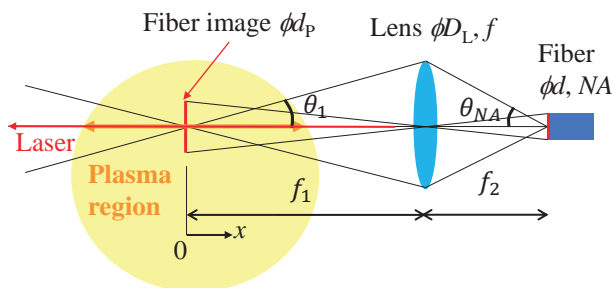


Fig. 1 Schematic drawing of a complete backscattering configuration with a lens and a fiber.

following, we will consider an ideal optical system for a given first lens location $x = f_1$ and diameter D_L . The fiber position should satisfy $D_L/(2f_2) \leq NA$ not to lose the scattering light which is generated at $x = 0$ and passes through the lens. When we consider the scattering light generated at $x \neq 0$, it should pass through the lens and the fiber entrance aperture to contribute the signal. The latter condition for the light to pass the fiber entrance aperture is equivalent to the condition for the light or backward extension of the light to pass through the fiber image at $x = 0$. The image diameter is equal to the product of the fiber diameter d and inverse of the magnification f_1/f_2 . Since the larger the image diameter is the higher efficiency is expected for the light generated at the position far from $x = 0$, a higher ratio f_1/f_2 is preferable. Combining this with the above obtained inequality: $D_L/(2f_2) \leq NA$, the recommended condition in terms of the line integrated measurement efficiency is written as

$$\frac{D_L}{2f_2} = NA. \quad (1)$$

Although this may not be the numerical optimum in a practical system, we choose this condition in the following analysis. The fiber image diameter is written as

$$d_p = \frac{f_1}{f_2} d = \frac{f_1 d}{D_L/2} NA. \quad (2)$$

The focal length of the lens becomes $f = (1/f_1 + 1/f_2)^{-1}$ when we neglect aberration. Note that the focal length cannot be determined uniquely for an actual optical component which has aberration. In order to compare the ideal optical system (without aberration) and a practical but simple system, the lens is replaced by a spherical concave mirror, in which we expect only the spherical aberration. In stead of the focal length f described above we adopted the following value:

$$f = \frac{D_L}{4} ((\sin(\theta_1 + \theta_{NA}))/2)^{-1}. \quad (3)$$

Here, θ_1 and θ_{NA} are the angles defined in Fig. 1. This focal length is that for the light passing through the edge of the mirror, while $f = (1/f_1 + 1/f_2)^{-1}$ is the focal length for paraxial rays. Equation (3) is better to locate the sensitivity peak closer to $x = 0$ as shown later. The reason for this is probably that the solid angle for edge region is larger than that for central region, and signal intensity is determined mainly by the behavior of the rays passing through the edge region.

Figure 2 shows the solid angle profiles $\Omega(x)$ obtained analytically and those calculated from ray tracing. Here, we assume a spherical concave mirror with diameter $D_L = 195$ mm located at $f_1 = 1032$ mm, and a fiber with diameter $d = 2$ mm and $NA = 0.37$. The fiber parameters are the same as those for the present TS systems in TST-2 and QUEST [5,6]. The mirror location and diameter were chosen so that it fits in an available space in TST-2, which is

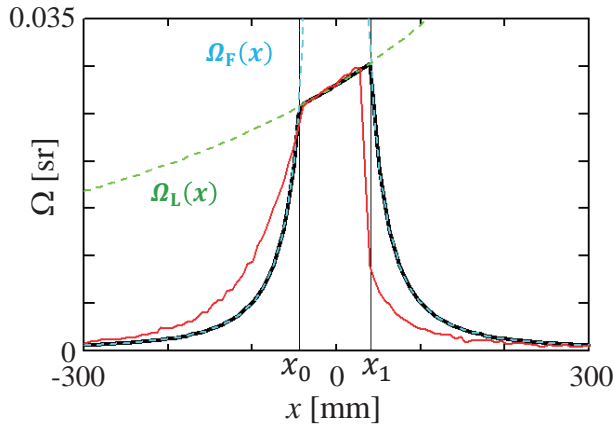


Fig. 2 Solid angle profile $\Omega(x)$. The results of a ray tracing calculation (red) and the analytic solution (black) are shown. The latter consists of two functions $\Omega_F(x)$ and $\Omega_L(x)$. The optical system parameters are $D_L = 195$ mm, $f_1 = 1032$ mm, $d = 2$ mm, $NA = 0.37$ ($D_L/f_2 = NA$).

shown later. The analytical $\Omega(x)$ consists of two functions: $\Omega_F(x)$ and $\Omega_L(x)$, which are written as

$$\Omega_F(x) \equiv \frac{\pi(d_p)^2}{x^2}, \quad \Omega_L(x) \equiv \frac{\pi(D_L/2)^2}{(f_1 - x)^2}. \quad (4)$$

The former function $\Omega_F(x)$ implies that scattering lights should pass through the fiber aperture (or fiber image at $x = 0$), and the latter function $\Omega_L(x)$ implies that the lights should pass through the mirror (or lens). While $\Omega_F(x)$ forms a peak at $x = 0$, $\Omega_L(x)$ imposes the upper limit around $x = 0$. The intersection of these two functions are located at $x_0 = f_1 d_p / (d_p - D_L)$ and $x_1 = f_1 d_p / (d_p + D_L)$. Usually $d_p < D_L$, and then $x_0 < 0$. When the lens (or mirror) is located far from the plasma (i.e., $|x| \ll f_1$, $\Omega_L(x)$ tends to be constant. Thus, the region $x_0 < x < x_1$ becomes quasi-line-integrated region. In the outside region, $\Omega(x)$ decreases quickly due to $1/x^2$ dependence of $\Omega_F(x)$, and this implies that the length $\Delta x \equiv x_1 - x_0$ is a measure of localization or spatial resolution. Δx is approximated by

$$\Delta x \equiv x_1 - x_0 \approx \frac{4f_1^2 dNA}{D_L^2}. \quad (5)$$

When Δx is much smaller than the plasma size localized measurement is possible, while quasi-line-integrated measurement is possible for the opposite case. f_1/D_L is the f-number of the lens (or mirror), and Δx is proportional to the square of this f-number. In the case of demo reactor, f-number would be as large as 25 ($L/r = 50$) and Δx can be longer than the plasma size. In TST-2, the f-number can be small, and f-number = 5.3 and $\Delta x = 82$ mm for the case shown in Fig. 2. The result of ray tracing calculation (red curve in Fig. 2) is partly approximated by the analytic expression, but the shoulder positions near $x = x_0$ and $x = x_1$ move due to spherical aberration of the concave spherical mirror. Since the spherical aberration itself can only move

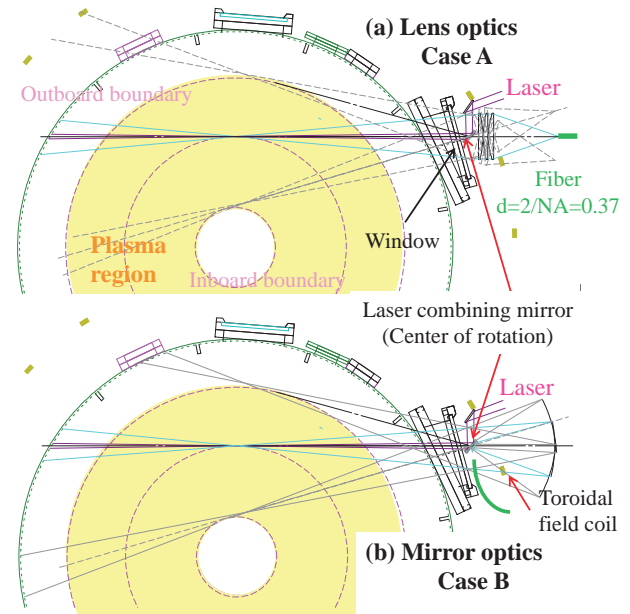


Fig. 3 TST-2 topview and the arrangements of the optics using three convex lenses Case A (a) and the optics using a spherical concave mirror Case B (b).

the focal points along the optical axis, the total solid angle $\int \Omega(x) dx$ is almost preserved. In the case of Fig. 2, the difference between the line integrated solid angle for the analytic and calculated ones is about 4%.

Figure 3 shows two systems in TST-2: one using three convex lenses and one using a spherical concave mirror. We chose three ready-made convex lenses (Edmund optics Inc., one #27-510 ($\phi 145$, $f = 450$ mm) and two #27-511s ($\phi 145$, $f = 600$ mm)) to form an efficient optical system (Case A: Fig. 3 (a)). For the spherical mirror in Case B, we set $\phi 195$, $f = 207.3$ mm. The focal length f was chosen to satisfy Eq. (1) for f_2 for given $f_1 = 1032$ mm and $D_L = 195$ mm. The sizes and locations of the optical components were chosen to fit in the place near the window. In order to reconstruct density or temperature profiles, we need to perform multi-chord measurements, each of which has a weight $\Omega(x)$ along the chord. One method for the multi-chord measurement is rotating the whole system to scan the chord. For that purpose, the lenses or the mirror should be rotated without touching the toroidal field coils (olive rectangles in Fig. 3) or other fixed structures. In Case A, the first lens should be located close to the window to maximize the solid angle. In Case B, the fiber should be located close to the window. In order to inject a laser beam along the axis of the collection optics an elliptic mirror (40 mm width and 50 mm height) is placed just in front of a large window ($\phi 215$) in TST-2. The (laser combining) mirror is tilted by 45 degrees from the optical axis and the projected shape along the axis is a circle ($\phi 40$), and the scattered light is partly masked by this mirror. The size is determined to reflect a Gaussian beam with the $1/e^2$ intensity radius of 10 mm. The waist size

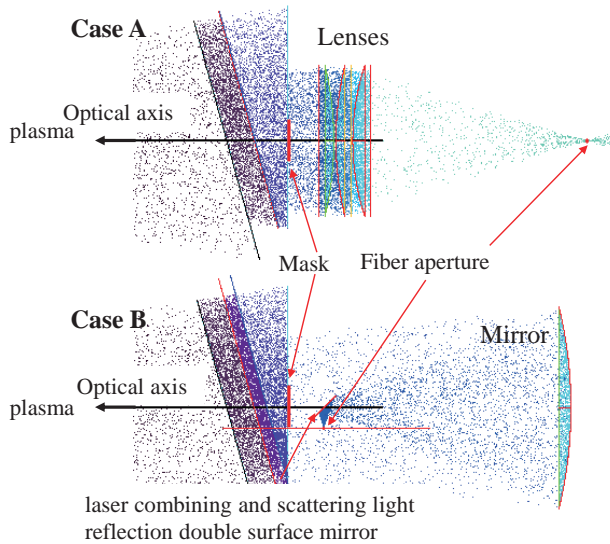


Fig. 4 Ray tracing results for Case A (black) and B (red) shown in Fig. 3. Rays are represented by dots.

at the focal point is about 0.025 mm and the size at the edge of the plasma ($x = 415$ mm) is about 5.5 mm. When the Gaussian beam radius is 10 mm and the laser energy is 1 J, the energy density becomes 0.64 J/cm^2 , which is much smaller than a typical AR coating of commercial products. For example, B coating products by Thorlabs Inc. have a laser damage threshold of 7.5 J/cm^2 . The mask effect and focusing Gaussian beam effect are considered later. In Case B, the opposite side of the laser combining mirror is used to reflect the collected light by 90 degrees, so that the fiber (with a minimum allowable curvature of 200-400 mm) does not hit the window. By rotating the collection optics and the laser combining mirror around the center of the laser combining mirror surface, we can change the measurement chord as shown in Fig. 3. Note that the rotation angles for the laser combining mirror and the collection optics are two times different.

Figure 4 shows rays in ray tracing calculations. To represent a ray, dots are used instead of a line. Dots are randomly and uniformly distributed along each ray, and a high dot density region represents the high intensity region near the focal points. In addition, dots are plotted at the points where each ray hit a surface of an optical component to show the 3D shape of the surface. The laser combining mirror in Case A is represented by a circular mask, while the collected light is reflected by the mirror in Case B. The window thickness is set to be 1 mm, while the actual window thickness is 12 mm. This thin window makes the calculation setup easy. A constant refractive index of 1.507 (for BK7 glass at 1064 nm) is assumed, and chromatic aberration is neglected in the present study. Note that the three commercial lenses are designed assuming a refractive index of 1.516 (for BK7 glass at 587.6 nm). The fiber aperture position is chosen to maximize the solid angle (i.e., efficiency) at $x = 0$. Many rays are calculated and

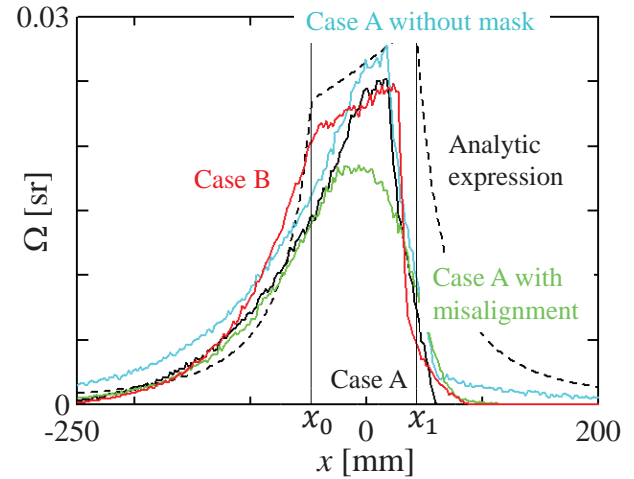


Fig. 5 Solid angle profiles $\Omega(x)$ for Case A (black), Case B (red) and Case A without mask (light blue) and with misalignment of 2 mm. An analytic solution for the case similar to Case A is shown by a dashed curve.

the rays passing through the optical components and hitting the fiber aperture with an angle within NA is counted to calculate the solid angle for a given x .

The solid angle profiles $\Omega(x)$ s for several cases are calculated by ray tracing. Figure 5 shows Case A, Case B and Case A without the mask effect (due to the laser combining mirror), and Case A with misalignment effect. An analytical solution for the case similar to Case A is shown by dashed curve. In the analytical solution case, we locate an ideal lens (i.e., thin lens without aberration) with the same diameter and with the same location as the first lens in Case A. This solution is the target $\Omega(x)$ for the present optical design. Case A is a baseline design, and we compare the other cases with this. The solid angle around the origin $x = 0$ is smaller than the analytic solution because of the laser combining mirror, by which a part of the scattered light is masked. The solid angle recover to the value of the analytic solution in Case A without mask. At the regions far from the origin, Case A without mask shows much larger Ω than Case A, and this phenomenon can be explained as follows. Since the mask (by the laser combining mirror) is located around the optical axis, this part contributes to increasing Δx defined by Eq. (5). This is the same phenomenon as that a larger f-number optical system has a deeper depth of focal. The reduction of Ω at the region is a disadvantage from the viewpoint of signal intensity, but it is advantageous from the viewpoint of localized measurement, because the long tail components in $\Omega(x)$ are eliminated. The localization is quite important and discussed in detail in the next section.

In general, the efficiency (i.e., effective solid angle) of an optical system is highest on the axis, and the misalignment between the laser beam axis and optical axis of the collection optics may induce a serious degradation of the efficiency. The effect of misalignment depends probably

on the misalignment distance normalized by the fiber image size d_p (Eq. (2)). In Case A, where $d_p = 8.1$ mm, we can expect the misalignment effects are not serious when the misalignment distance is much smaller than d_p . Here, we assume that the laser beam is apart from the optical axis by 2 mm in Case A with misalignment (green curve in Fig. 5). This 2 mm is larger than those we can usually achieve, but we adopt it to show the difference clearly. We adopt 1 mm as a more realistic value in the next section. The solid angle decreases at $x \sim 0$ because the focal points on the fiber aperture shifts, while the solid angle far from the origin is almost the same as Case A without misalignment. $\Omega(x)$ for the Gaussian laser beam (with the waist size of 0.025 mm at $x = 0$ and the beam size of 10 mm at the window) is not shown, because the curve almost overlaps with that of Case A.

The profile of Case B shown in Fig. 5 is almost the same as the red curve in Fig. 2, but due to the laser combining mirror, a part of the scattered light is masked, and the solid angle decreases slightly. It is not easy to determine which of Case A (lens system) and Case B (mirror system) is superior. One practical point is that the finite thickness of the laser combining mirror causes a shift of optical axis on the back surface when we rotate the system around the center of the front surface, and vice versa. The shift may introduce additional misalignment. Another option for Case B is not to use the back surface to reflect the collected light toward the fiber. Then the fiber should be located behind the laser combining mirror, and we need additional space along the optical axis to locate the fiber. As a result, the system becomes larger and the efficiency is probably deteriorated. Thus, Case A seems to be simpler.

3. Profile Reconstruction and Its Error

Since the present complete backscattering configuration is a line integrated measurement with weight $\Omega(x)$, a profile reconstruction from multi-chord measurements is necessary. In this section, we investigate the error in resultant reconstructed density profiles under several assumptions. Firstly, a multi-chord measurement, each chord of which is tangent to a certain magnetic surface (see Fig. 3), is discussed. Secondly, reconstruction from axial scan measurement is discussed. Here, we discuss only density profile reconstruction, and we do not discuss temperature profile reconstruction. Since temperature is a function of the ratio of signals at (two) different wavelength regions, the error of the ratio can be minimized when we set appropriate wavelength regions. As a result, the relative temperature error becomes similar to the relative density error [3].

Figure 6 shows schematic configuration for profile reconstruction. Due to the axisymmetric tokamak configuration, the density profile at the midplane is a function of major radius R , and we consider a density profile reconstruction from a multi-chord measurement on the mid-

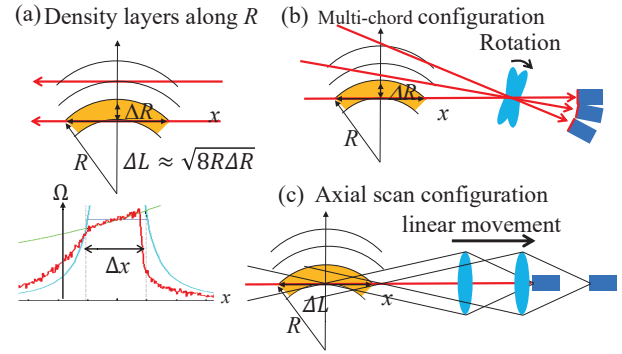


Fig. 6 Schematic configurations for profile reconstruction. The relationship between the weight along a chord and the density layers (a), a multi-chord measurement configuration (b) and an axial scan configuration (c) are shown.

plane. The profile is represented by several discrete R s and we adopt multi-layer model for the density, in which the density in each layer (with thickness ΔR) is constant. A measurement chord passes through many layers and the chord is tangent to a magnetic surface at the innermost layer. Then the length ΔL in the inner most layer is approximated by

$$\Delta L \approx \sqrt{8R\Delta R}. \quad (6)$$

Note that $\Delta L \gg \Delta R$. The weight $\Omega(x)$ is high at the origin (focal points) and the width of the large weight region is represented by Δx (Eq. (5)). If $\Delta x \ll \Delta L$, then we can do localized measurement for a given ΔR without any reconstruction. In practice, $\Delta x \sim \Delta L$ and a quantitative analysis is necessary.

Firstly, we consider a multi-chord measurement, in which the optical axis of the whole system is rotated around a point as shown in Fig. 6(b). The point is the center of the laser combining mirror surface in Case A (Fig. 3 (a)). Suppose the system is rotated on shot by shot basis, and 20 chords are measured using 20 reproducible plasmas. Each chord is labeled by the tangent radius R_{Ti} ($i = 1, \dots, 20$). For a given R_{Ti} , the major radius is a function of coordinate x along the chord, and it is expressed as $R(x; R_{Ti})$. Figures 7 (a) and (b) show $\Omega(x)$ and major radius $R(x; R_{Ti})$ for 20 chords, respectively. The combination of $\Omega(x)$ and $R(x; R_{Ti})$ yields the measurement weight in R . To simplify the analysis, here, we assume $\Omega(x)$ is the same for all chords. In practice, it would become small at large R_T in Case A (Fig. 3 (a)), because the window is not large enough.

When the (electron) density profile $n(R)$ is given, each point on the chord contributes to the signal with efficiency (i.e., weight) $\Omega(x)$. Since the TS signal is proportional to the density, the signal s_i is written as

$$s_i = \int \Omega(x)n(R(x; R_{Ti}))dx. \quad (7)$$

In order to simplify the discussion, here, we assume the

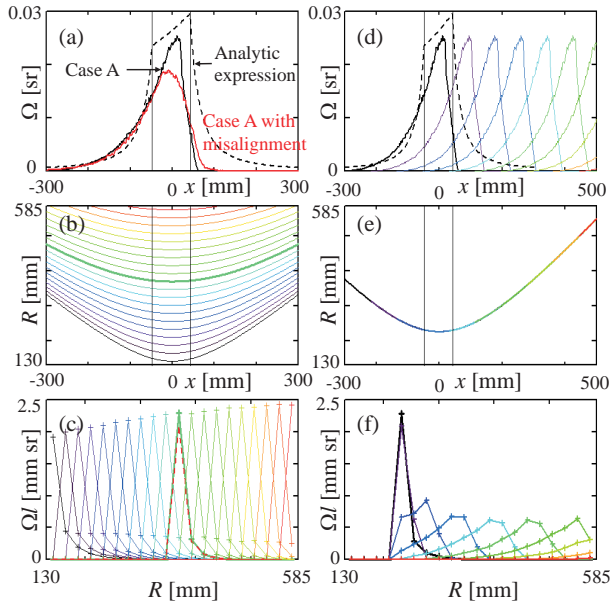


Fig. 7 $\Omega(x)$ for Case A and Case A with a misalignment of 2 mm (a), major radius $R(x; R_T)$ for 20 chords (b), contribution L_{ij} of layers to each signal as a function of layer center radius R_j (c). Different colors in (b) and (c) represent the curves (or connected lines) for different chords. The thick green curves (or connected lines) in (b) and (c) represent the case $R_T = 369$ mm. The L_{ij} using the $\Omega(x)$ with the misalignment is shown by dashed red lines in (c). While (a), (b) and (c) are used for profile reconstruction by the multi-chord configuration (Fig. 6 (b)), (d), (e) and (f) are used for reconstruction by the axial scan configuration (Fig. 6 (c)). The thick black curve or lines in (d) and (f) represent the case with $R_T = 225$ mm with no shift along x .

density profile is discretized by 20 (or 12) layers in which the density is constant. We will adopt 12 layers for the axial scan configuration later. Thus, the density profile is represented by 20 unknown variables: n_j ($j = 1, \dots, 20$), and the problem becomes solving simultaneous linear equations:

$$s = Ln. \quad (8)$$

Here, s and n are the signals and densities in vector forms. L is a matrix with element L_{ij} , which represents the contribution of j -th density layer to i -th signal (Fig. 7 (c)). A set of connected lines L_{ij} ($j = 1, \dots, 20$) represents a chord measurement with weights Ωl of density layers. Thus, its shape represent the localization, and it is a few points along the major radius in the cases shown in Fig. 7 (c). This relatively good localization is due to the localization along x and tangent chords (Figs. 7 (a) and (b)).

A case with misalignment of 2 mm is shown in Fig. 7 (c). The peak is reduced by about 25%, and the total area ($\int \Omega(x) dx$) is reduced by 8%. The major effect of misalignment is the reduction of reconstructed density due to the decreased Ω . We will assume a misalignment of 1 mm later, because 1 mm is more practical in our experi-

ences, and the reductions for this case are 8% and 2% for the peak and the total, respectively. Equation (8) can be solved by using the inverse matrix L^{-1} , however, the stability of the solution against noise or perturbation should be investigated. Note that this method is a variation of the standard slice and stack method, which is often used for the density profile reconstruction from line integrated microwave or laser interferometer measurements [7]. The stability depends on individual matrix L . In general, it is easy to obtain the inverse matrix of a diagonal matrix, and this is the localized measurement case. In the case of a multi-chord configuration, the matrix becomes a upper triangular matrix, and the off diagonal components tend to enhance the errors. The effects on the reconstructed density profile are described later.

The vertical axis Ωl in Fig. 7 (c) represents the efficiency of measurements, and this quantity is often used to represents the performance of a TS configuration. The values are around 2 mm sr, which is much larger than the values of 0.1 - 0.42 mm sr in the present conventional TS system in TST-2 [8]. It should be noted that l in this paper depends on the number of density layers (i.e., spatial points along the major radius) and a strict comparison is difficult, but this large Ωl is very attractive when we want to measure very low density plasmas [9].

Since $\Omega(x)$ itself has a width of about 100 mm, we can expect weakly localized measurements. Figure 6 (c) shows the axial scan configuration, in which the whole system is scanned along the optical axis with a fixed tangent radius R_T . This configuration is attractive from the viewpoints of implementation, because it is simpler and alignment between the laser beam and the optical axis seems to be easier than the multi-chord configuration which requires rotation. Then the the solid angle profile becomes $\Omega(x - \Delta x)$ for the movement of Δx . $\Omega(x - \Delta x)$ and $R(x; R_T = 225$ mm) are shown in Figs. 7 (d) and (e), respectively. The corresponding L_{ij} as a function of R_j is shown in Fig. 7 (d). In this configuration we assume 12 density layers. Here, we adopt 12 instead of 20 to improve the stability (i.e., to reduce the effects of noise). Although the L_{ij} for $\Delta x = 0$ is well-localized, the other L_{ij} s (for $\Delta x \neq 0$) are spread over different R_j s, and they are poorly localized, leading to a poor reconstruction performance as shown later.

The stability (or the performance) of reconstruction can be shown by the errors of reconstructed profile for given noises. The profile is assumed to be a parabolic density profile with a peak height of 1, filling the region between the inboard limiter at $R = 130$ mm and the outboard limiter at $R = 585$ mm. Firstly, artificial signals are calculated by Eq. (7), and then, Gaussian random noises with the relative amplitude of 10% are added. Reconstructed profiles are obtained by multiplying the inverse matrix L^{-1} . We do not impose any constraints, such as smoothness, on the profile to see the intrinsic performance of the methods. Figure 8 (a) shows the original parabolic density profile, reconstructed profiles with and without noises. The profile

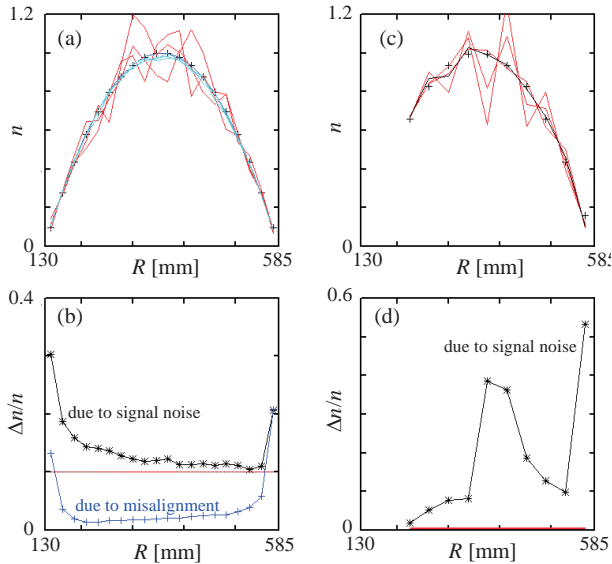


Fig. 8 Reconstructed density profiles ($n(R_j)$) by the multi-chord configuration (a) and the relative density errors $\Delta n/n$ (b). (c) and (d) shows those for the axial scan configuration measurement. Plus (+) symbols in (a) and (c) show the original density profiles. Red lines in (a) and (c) are the profiles with noises (10% for (a) and 0.5% for (c)) in the signals. Light blue lines in (a) are the profiles with Gaussian misalignment with the standard deviation of 1 mm. Red horizontal lines in (b) and (d) shows the levels of 10% and 0.5% as guide lines.

without noise agree with the original profile, but the profile with noise deviate from the original one. In order to evaluate the noise effect we calculated rms deviation from the original density Δn from many samples with the Gaussian random noises. The relative noises $\Delta n/n$ is slightly larger than the relative noise of 10% (in the signals) at most R_j s, but the relative noise increases with the decrease in R_j (Fig. 8 (b)). This is partly due to the accumulated noise effects, which is often seen in the profile reconstruction from line integrated measurements.

The large relative error near the inboard limiter is mainly due to the low density near the inboard limiter. Due to the line integration effect, the inner density is affected by the outer densities and about 10% error in the outer higher densities cause a large relative error in the inner lower density. The discretization induces additional relative errors near the boundaries, because the original density varies quickly near the boundaries and systematic differences between the integrals of original continuous density and the discrete density arises. As shown by the green curve in Fig. 5, misalignment degrades the sensitivities in most of the x region. Therefore, both the line integrated signal and the reconstructed profile decrease (light blue lines in Fig. 8 (a)). Now, we assume random misalignments with a Gaussian distribution with the standard deviation of 1 mm. The effects on $\Delta n/n$ are less than 3% (plus symbols in Fig. 8 (b)). When we consider both the signal noise and

the misalignment, the resultant $\Delta n/n$ roughly follows the summation rule of independent errors, and it is mainly determined by the signal noise in this case. As a result, the profile reconstruction by the multi-chord configuration is possible, and there is little excess deterioration in the performance.

In the case of the axial scan configuration, the localization is very poor as shown in Fig. 7 (f). Figure 8 (c) shows the original (+ symbols) and reconstructed profile without noise (black lines). Even without noise, the reconstructed profile deviates systematically from the original one due to the discretization. This deviation is sensitive to the setup of the layers. The effect of random error in signals is serious, and 0.5% error in the signals causes 40% relative error in the reconstructed density. These results indicate that this axial scan configuration is not attractive, although we can improve the performance by using a more sophisticated method.

4. Conclusions

A design study of a line integrated TS system with a complete backscattering configuration has been performed to clarify practical problems. Installation on the TST-2 spherical tokamak was assumed, and a design which fits in a place near a large window was adopted. The collection optics consists of three ready-made convex lenses (with diameters of 150 mm), and the laser beam is aligned to the axis of the collection optics by a small mirror located near the lenses. One of the important performances of the system is the spatial localization of the measurement, and some analytic expressions are obtained for an ideal system characterized by the first collection lens' location and diameter and the fiber's diameter and NA. Some practical aspects of a system, such as aberration, masking effect of the laser combining mirror, misalignment, are investigated by ray tracing calculations. The performance of (density) profile reconstruction was investigated for two configurations. A tangential-multi-chord measurement configuration on the midplane shows a relatively good localization (~ 100 mm) around the tangent points, and error (i.e., noise) enhancement in the reconstruction is small. In addition, the effective efficiency of the system is about an order of magnitude larger than the present conventional TS system. An axial scan configuration, which can be easily implemented, shows a poor localization, and error enhancement is so serious that the configuration is impractical. In conclusion, quantitative performance and various practical aspects were clarified through the present design study, and attractiveness of the line integrated TS system was demonstrated. It should be noted that the effect of stray light is difficult to estimate and it would be a future task, but the complete backscattering configuration mitigate the effect by increasing the Doppler shift.

Acknowledgement

This work is supported by National Institute for Fusion Science Collaboration Research Programs NIFS20KUTR155 and NIFS22KIPP007.

- [1] W. Biel *et al.*, Fusion Eng. Des. **146**, 465 (2019).
- [2] K. Tobita *et al.*, Fusion Sci. Technol. **75**, 372 (2019).
- [3] Y. Lin *et al.*, Plasma Fusion Res. **17**, 1405098 (2022).
- [4] Y. Takase *et al.*, Nucl. Fusion **41**, 1543 (2001).
- [5] T. Yamaguchi *et al.*, Plasma Fusion Res. **5**, S2092 (2010).
- [6] T. Yamaguchi *et al.*, Plasma Fusion Res. **8**, 1302001 (2013).
- [7] e.g. H.K. Park, Plasma Phys. Control. Fusion **31**, 2035 (1989).
- [8] J. Hiratsuka *et al.*, Plasma Fusion Res. **7**, 2402092 (2012).
- [9] H. Togashi *et al.*, Plasma Fusion Res. **10**, 1202082 (2015).